Submitted to the Journal of Biomechanics

Efficient development of subject-specific finite element knee models: Automated identification of soft-tissue attachments

Vahid Malbouby[1], Kalin D. Gibbons[1], Nurbanu Bursa[2], Amanda K. Ivy[1], Clare K. Fitzpatrick[1]

[1] Mechanical and Biomedical Engineering, Boise State University, Boise, ID

[2] Biomedical Research Institute, Boise State University, Boise, ID

Corresponding Author: Clare K. Fitzpatrick, PhD
Mechanical and Biomedical Engineering
Boise State University
1910 University Drive, MS-2085
Boise, ID 83725-2085
Phone: 1 + 208.426.4027
Fax: 1 + 208.392.1589
Email: clarefitzpatrick@boisestate.edu

ABSTRACT:

Musculoskeletal disorders impact quality of life and incur substantial socio-economic costs. While in vivo and in vitro studies provide valuable insights, they are often limited by invasiveness and logistical constraints. Finite element (FE) analysis offers a non-invasive, cost-effective alternative for studying joint mechanics. This study introduces a fully automated algorithm for identifying soft-tissue attachment sites to streamline the creation of subject-specific FE knee models from magnetic resonance images. Twelve knees were selected from the Osteoarthritis Initiative database and segmented to create 3D meshes of bone and cartilage. Attachment sites were identified in three conditions: manually by two evaluators and via our automated Python-based algorithm. All knees underwent FE simulations of a 90° flexion-extension cycle, and 68 kinematic, force, contact, stress and strain outputs were extracted. The automated process was compared against manual identification to assess intra-operator variability. The attachment site locations were consistent across all three conditions, with average distances of 3.0 ± 0.5 to 3.1 ± 0.6 mm and no significant differences between conditions ($p=0.90$). FE outputs were analyzed using Pearson correlation coefficients, randomized mean squared error, and pairwise dynamic time warping in conjunction with ANOVA and Kruskal-Wallis. There were no statistical differences in pairwise comparisons of 67 of 68 FE output variables, demonstrating the automated method's consistency with manual identification. Our automated approach significantly reduces processing time from hours to seconds, facilitating large-scale studies and enhancing reproducibility in biomechanical research. This advancement holds promise for broader clinical and research applications, supporting the efficient development of personalized musculoskeletal models.

KEYWORDS: finite element, knee, subject-specific modeling, ligament attachments, automated

INTRODUCTION:

Musculoskeletal disorders are a principal cause of discomfort, disability, and diminished quality of life globally, bearing considerable socio-economic consequences. The study of musculoskeletal disorders encompasses three primary methodologies: in vivo, in vitro, and in silico investigations. In vivo research, while offering direct insights, often entails invasive procedures, and it can be difficult to properly capture the mechanical environment of musculoskeletal structures (Cooper et al., 2019). Cadaveric studies, provide more structural clarity but they lack the muscular tone and other dynamic properties of some living tissues (Wang et al., 2023). Both experimental approaches face constraints related to time, financial, and logistical factors, including the scarcity of subjects or specimens. Computational analysis is a potential alternative to in vivo and in vitro investigations. It is typically more efficient and cost effective and can be applied on a broader scale than these methods (Diamond et al., 2024). Nonetheless, there are challenges associated with the effort and expertise required to develop subject-specific computational models (Paz et al., 2021).

Finite element (FE) analyses are commonly used in orthopedic applications to simulate complex dynamics of joints and muscles (Pfeiffer, 2016). FE studies include optimizing design and positioning of knee implants (Dagneaux et al., 2024), investigating spinal disc degeneration (Khuyagbaatar et al., 2024), analyzing foot and ankle injuries (Phan et al., 2021), exploring shoulder stability and rotator cuff tears (Zheng et al., 2017), studying hip impingement (Ng et al., 2016), and osteoarthritis research (Diamond et al., 2024). This method can include detailed, subject-specific, anatomic representations, mechanical properties and complex loading and boundary conditions. FE simulations allow for detailed assessments of stress and strain distributions within tissues, as well as joint contact forces and kinematics (Erdemir et al., 2019).

Many studies use a singular, representative anatomic model of a joint, which neglects the inherent variability among individuals, potentially skewing analysis results and limiting their general applicability across the broader population (Taylor et al., 2013). More recently, there has been a transition towards subject-specific FE modeling (Ellis et al., 2010; Lochner et al., 2014; Mononen et al., 2016; Ng et al., 2012; Rieger et al., 2024; Worsley et al., 2011). Incorporating subject-specific properties generally enhances the predictive accuracy of the models, making their outcomes more congruent with experimental results (Naghibi Beidokhti et al., 2017). High degrees of subject-specificity in FE models, however, often necessitate limiting the study to a smaller cohort due to constraints on time and resources (Ali et al., 2017; Cooper et al., 2019; Harris et al., 2016; Naghibi Beidokhti et al., 2017). Conversely, studies that manage to include a larger sample size tend to rely on more generalized information or employ parametrized models (Cooper et al., 2018; Mononen et al., 2023), which may not capture the individual variability as effectively.

The challenge of incorporating large sample sizes in subject-specific computational modeling has been underscored in recent review papers: within FE studies focusing on osteoarthritis research, only three incorporated more than 20 subjects from 2020 to 2021 (Harlaar et al., 2022) and only one study incorporated more than 30 participants in 2022 (Diamond et al., 2024). This highlights the ongoing need for methodological advancements that can reconcile the demand for both individual specificity and broad population applicability in FE studies on musculoskeletal disorders.

Advancements in machine learning techniques have significantly reduced the necessity for manual processing and segmentation of medical images to create 3D meshes of bones and cartilages, thereby diminishing the time required for this task from days to minutes (Ambellan et

al., 2019; Burton et al., 2020; Ebrahimkhani et al., 2020; Esrafilian et al., 2023; Gibbons et al., 2022). Initially, most of these studies focused on bone, cartilage and menisci, and did not include tendon and ligament representations. Manual identification of attachment sites, whether derived directly from medical imaging or based on anatomical descriptions, can be time consuming and is susceptible to significant intra-operator variability, thus impacting the reproducibility of the data. Recently, several automated pipelines for identifying tendon and ligament attachment sites on a 3D joint model have been developed (Clouthier et al., 2022, 2019; Esrafilian et al., 2023, 2020; Killen et al., 2024; Willems et al., 2024). However, to the best of our knowledge, no previous work has evaluated the performance of these approaches to a human operator. Thus, the effectiveness and reliability of these automatic algorithms compared to the manual selection of these sites remain unknown.

The primary objective of our study is to introduce a novel, fully automated algorithm that facilitates the rapid and accurate identification of attachment sites for use in FE simulations, and compare it to the traditional manual method. For this, we compare FE outputs from our automated process with those from models with manually identified soft tissues. A fully automated algorithm will streamline the construction of musculoskeletal models and reduce the time for identification of attachment sites to just a few seconds, thereby enabling broader application in clinical and research settings.

METHODS:

Data sources. Twelve knees were randomly selected using the 'sample' function in Python from the Osteoarthritis Initiative (OAI) database (NIAMS, 2004), based on the availability of the

subject's weight, femoral and tibial lengths, double echo steady-state (DESS) magnetic resonance (MR) images, and a Kellgren-Lawrence (KL) grade of less than 2. The MR images consisted of 384×384×160 voxels and featured a spatial resolution of 0.37×0.37×0.70 mm in the sagittal plane. MR scans were manually segmented using AMIRA software, and 3D FE meshes were created for the femur, tibia, patella, and their corresponding cartilages (Gibbons et al., 2022). Bones were meshed using uniform triangular rigid body surface meshes with a target element size of 3 mm, while cartilage employed four layers of deformable hexahedral elements with an average element edge length of 1 mm and blended edges (Gibbons et al., 2022) and isotropic elastic material properties similar to prior models (Fitzpatrick et al., 2014, 2012; Klets et al., 2016).

Manual attachment site identification. All knees were manually processed to identify ligament and muscle attachment sites by two evaluators, each blinded to the other's work and to the automatic processing (described in the subsequent section). Both raters had similar levels of experience (multiple years) in manually reconstructing knee MR images and identifying attachments to develop FE models. This approach allowed for the assessment of intra-operator variation, providing a benchmark for the automated method's performance. The attachment sites of interest were: origins and insertions for the anterior and posterior cruciate ligament (ACL, PCL), superficial and deep medial collateral ligament (MCL, dMCL), lateral collateral ligaments (LCL), medial and lateral patellofemoral ligaments (MPFL, LPFL), anterolateral structure (ALS), patellar ligament (PL), posterior oblique ligament (POL), popliteofibular ligaments (PFL), and lateral and medial posterior capsule ligaments (mPCAP, lPCAL), along with those for the vastus lateralis and medialis (VL, VM), a combined bundle for vastus intermedius and rectus femoris (VI+RF), long and short head of biceps femoris (BFLH, BFSH), semitendinosus (ST),

and semimembranosus (SM) muscles (Figure 1). ACL and PCL were modeled using four springs each, POL was modeled using two springs, and other structures were modeled using three springs, except for muscles and PL. The VI+RF and PL were modeled using six springs each, while hamstring muscles were modeled using one spring per bundle. These were chosen based on a combined cadaveric and experimental study, where they found that this fiber selection used in their computational study provided excellent agreement with the laxity data from the experiment (Harris et al., 2016). This ligament template was used by both manual evaluators and the automated algorithm.

Automated attachment site identification. For the automated identification of attachment sites, the same reference template was used (Harris et al., 2016) in conjunction with a Python-based algorithm to select the optimal attachment sites on the subject's knee. The distal femur and proximal tibia were aligned with their corresponding bone segments in the template using an iterative closest point (ICP) algorithm from the Open3D library (Zhou et al., 2018). For femur and tibia, each bone was scaled independently to best-match the medial-lateral and anterior-posterior dimensions of the template model, and the superior-inferior axis was scaled based on the average of these two dimensions to prevent the shaft length on the MR images from affecting the transformation. The patella was scaled in all three dimensions separately to ensure alignment with the template dimensions.

For each attachment point on the template model, nearby nodes—'template anchor nodes'—are identified using a nearest neighbor search with a unique predefined search radius for each site. Vectors from these nodes to the attachment points are stored and later scaled to match the dimensions between the template and subject bones. These vectors are applied to corresponding 'subject anchor nodes' on the subject model, identified through a similar search to match each

template anchor node to a similar node on the subject bone model. The subject attachment points are then determined by averaging these vector endpoints, weighted by the proximity of each point to the original attachment point in a logarithmic scale (Figure 2).

After attachment sites have been identified, each subject-specific model is aligned to a consistent local femoral coordinate system. A local tibial coordinate system was defined on the tibia based on anatomic landmarks. This was achieved via another automated algorithm finding the most distal contacting positions on medial and lateral femoral condyles and their corresponding dwell points on medial and lateral tibial condyles, and medial and lateral tibial intercondylar tubercles (Figure 3.A-C). Grood and Suntay (Grood and Suntay, 1983) axes were determined using a similar process, relying on established local origins for each of these bones and the unit vectors for medial-lateral, superior-inferior, and anterior-posterior directions (Figure 3.D).

FE model. The FE model employed in this study was modified from a previously published model (Fitzpatrick et al., 2014, 2012; Gibbons et al., 2022, 2019). Briefly, the model comprises the femur, tibia and patella bone and cartilage. The ligaments are modeled as nonlinear tension-only springs connecting the origin and insertion nodes identified as described above (Baldwin et al., 2012). The quadriceps muscles were modeled as three bundles with their line of action being based on cadaveric data (Farahmand et al., 2004): VI+RF, VM, and VL. The hamstring muscles, comprising SM, ST, BFSH, and BFLH, were represented by four non-linear spring connectors. Muscle activation was controlled via load actuators developed through a Fortran-based subroutine, distributing force according to average cross-sectional areas derived from cadaveric studies (Farahmand et al., 2004, 1998). The quadriceps muscle-tendon units were modeled using 2-D fiber-reinforced membrane elements to facilitate contact and wrapping during flexion. The load actuators were governed by proportional- integral (PI) controllers. The quadriceps controller

was set to align knee flexion with an average kinematic profile from in vivo studies of five participants performing a deep knee bend (Heinlein et al., 2007; Kutzner et al., 2010). The hamstring controller was adjusted to target a flexion angle 5° less than that of the quadriceps to simulate hamstring coactivation.

A vertical load equivalent to half of the subject's body weight was applied at the hip. An anterior-posterior load amplitude was applied to femur while its internal-external and varus-valgus rotation were constrained. The femur was free in other degrees of freedom. Internal-external and varus-valgus moments were applied to the tibia, with all other degrees of freedom constrained. The patella was free to move in all six degrees of freedom, with constraints imposed only by the articulating surfaces and connecting muscles and ligaments. Kinetic profiles for this model were derived from published telemetric data averaged across five patients performing a deep knee bend (Heinlein et al., 2007; Kutzner et al., 2010).

Output variables. FE model outputs included tibiofemoral (TF) and patellofemoral (PF) Grood and Suntay kinematics in all 6 degrees of freedom, quadriceps and hamstrings force, total axial force in the ACL ligament, total force on medial and lateral tibial condyles, total contact area on articulating surfaces of medial and lateral tibial cartilage and patellar cartilage, total force due to contact pressure, and the location of the center of pressure on these cartilages. Von Mises stress and first principal logarithmic strain were extracted for all elements on femoral, tibial, and patellar cartilage structures. We calculated the 50^{th} percentile and interquartile range across the knee bend activity for all cartilage elements. Additionally, we calculated the 90^{th} and 95^{th} percentiles for these variables, which are relevant in cartilage damage and degradation studies.

Statistical analysis. First, the Euclidian distances between the location for each node in the three conditions were calculated. These between-condition distances had normal distribution based on

a Shapiro-Wilk test and were analyzed via ANOVA across all subjects. Further statistical analysis was conducted on a dataset containing 68 output variables for each subject under each condition (Auto, Evaluator 1, Evaluator 2). Since all output variables were recorded as time series over the full flexion-extension cycle rather than as single values, dynamic time warping (DTW) was employed as an appropriate statistical method to compare conditions. DTW is a robust approach for determining the distance between two time series. The primary concept of DTW is to calculate the distance by comparing corresponding items in time series that are similar. DTW is scale sensitive and smaller DTW distances indicate greater similarity between the two series with the same unit (Gulzar, 2018; Müller, 2007). By comparing the DTW distances, we test if the variation between the auto model versus the manual models is within the same level of variation that exists between the two manual models.

First, pairwise DTW was used to compare the three conditions for each variable in each subject separately. Following this, a Shapiro-Wilk test of normality was performed for each condition. Based on the results, conditions were compared using either ANOVA or its nonparametric equivalent, Kruskal-Wallis test (Figure 4). All DTW analyses were conducted using R software (v4.1.3; R Core Team 2021) with the RStudio graphical interface. For the DTW tests, the "dtw" package was utilized (Giorgino, 2009). A two-sided p-value of less than 0.05 was considered statistically significant for all tests. Similarly, the root mean squared error (RMSE) comparing each subject across each pair of conditions was calculated for all variables and analyzed using either ANOVA or Kruskal-Wallis tests. The Pearson correlation coefficient (CC) was also calculated for all conditions and analyzed in the same manner. The aim of all three previous analyses was to determine whether the difference between two given conditions was statistically

significant compared to the other comparisons. All statistical analyses were conducted in python, using the SciPy package (Virtanen et al., 2020).

RESULTS:

The attachment site identification algorithm generated soft tissue representations in 8-10 seconds for each subject-specific FE model. The manual attachment site identification process took 4-6 hours for each subject, similarly for both evaluators. FE simulations for all subject-specific models were completed successfully (Figure 5).

Comparing spatial location for each attachment site between conditions across all subjects showed a mean distance of 3.0 ± 0.37 mm between evaluator 1 (E1) and evaluator 2 (E2), 3.1 ± 0.6 mm between E1 and auto (AU), and 3.0 ± 0.5 mm between E2 and AU (Figure 6). The between-condition distances were not statistically different in any pairwise comparison (p = 0.90).

The Pearson CC showed an average correlation of 0.96 ± 0.06 for the comparison between the two evaluators (E1-E2) across all variables, and 0.96 ± 0.07 for both evaluator-automatic comparisons (Figure 7). Independent statistical analysis for all variables showed no difference between the coefficients across conditions ($p>0.05$). There was no statistical difference between the pairwise RSME values across all variables ($p>0.05$), except for PF medial-lateral movement ($p=0.02$) (Figure 6). The CC and RMSE for all variables along with their relevant p-values for comparisons can be found in Appendix 1.

For the DTW tests comparing the outputs of the three conditions, none of the between conditions differences were significantly different than the other two across 67 out of the 68 variables ($p >$

0.05), except for PF medial-lateral kinematics ($p = 0.03$). The statistically significant difference for PF medial-lateral movement was not clinically meaningful, with mean PF medial-lateral differences between conditions being less that one millimeter (0.3-0.6 mm) across the entire flexion-extension cycle. Additionally, the DTW differences and RMSE values for patella contact area ($p = 0.36$ and 0.13, respectively), patella medial-lateral ($p = 0.51$ and 0.20) and superior-inferior ($p = 0.98$ and 0.94) center of pressure, as well as all other patellar force, strain, or stress outputs were not statistically different across conditions, demonstrating that this level of patella medial-lateral differences did not have any observable effect on joint mechanics.

Overall, the pairwise RMSE values and DTW differences between the manual models and the automatically created model for 67 out of the 68 variables tested, and the CC values for all 68 variables, were not statistically different throughout the entire flexion-extension range (Figures 8-10).

DISCUSSION:

The construction of subject-specific FE models of human joints entails several critical steps, including the acquisition of medical images, creation of 3D geometries from these images, conversion of the 3D geometries into a computational mesh, building the musculoskeletal model through identification of tendon and ligament origin and insertion points, determination of material models for different tissues, and application of kinematic and/or load profiles to the model, among other steps. With the recent advances in automatic processing of medical images to identify bone and cartilage geometries (Ambellan et al., 2019; Burton et al., 2020; Ebrahimkhani et al., 2020; Esrafilian et al., 2023; Gibbons et al., 2022), identification of tendon

and ligament attachment sites has emerged as the next challenge in developing automated pipelines to generate FE models from medical imaging.

Our results indicate that the two manual methods and the automated method demonstrated similar performance in determining attachment sites, as evidenced by the consistency in their geometric locations and their comparable impact on the biomechanics of the knee joint models across 67 kinematic and kinetic variables. The only variable where a significant difference between pairwise comparisons was found was for PF medial-lateral translation; however, the actual difference was less than one millimeter and did not affect relevant joint mechanics. Nevertheless, in 67 out of the 68 cases the variability between the automatically created model and the manually created models were within the same range of variability that exists between the manually created models, as evident by lack of a significant difference in the DTW and RMSE analysis. These data support our hypothesis that the automatic attachment site identification algorithm has a similar performance compared to a human evaluator. In the current work, we cannot evaluate the performance of these models against a single, gold-standard 'true' value; Comparing the outputs from these models to a clinically validated model of the same subject would create the possibility of evaluating the true performance of these models, but this would require additional data that was not available in our datasets and would be beyond the scope of this study.

The automated methods offer a consistent and objective alternative to manual identification, which can vary significantly between operators due to subjective interpretations and individual levels of expertise. This consistency enhances reproducibility in biomechanical research and clinical applications by removing the variability and inter-operator and between-operator errors introduced by human operators.

There has been a recent interest in the development of automated model segmentation and attachment site identification algorithms (Clouthier et al., 2022, 2019; Esrafilian et al., 2023, 2020; Killen et al., 2024; Willems et al., 2024). Esrafilian et.al. (2023, 2020) attempted to streamline the musculoskeletal attachment site identification for a FE simulation of human knee. One strength of their work was the identification of the insertion points for several ligaments and the quadriceps tendon based on auto-segmentation and reconstruction of their geometries from the MR images which can offer highly personalized musculoskeletal models, but given the challenges for auto-segmentation of these structures and poor performance for some ligaments, this algorithm reverts to extracting some locations from a template instead (Esrafilian et al., 2023). Clouthier et.al. (2022, 2019) used a statistical shape model with ligament and muscle attachment points which morphed along with bony geometry changes (Clouthier et al., 2019). Killen et.al. (2024) used a similar approach and continued further to project the attachment sites on the morphed model onto the personalized bone geometry. This approach has the potential of offering high accuracy, but the authors do not provide any validation or quantitative comparison against traditional manual attachment site identification. Also, this level of precision in replicating the template attachment locations comes at the price of computational efficiency, since the generation of each model takes several hours using this approach (Killen et al., 2024). In our proposed algorithm, the generation of each model takes 8-10 seconds, and to the best of authors' knowledge, this is the first time that quantitative evaluations of performance and similarity to the manual method have been presented for an automated attachment site identification algorithm.

One limitation of this study is our reliance on manual identification as a benchmark as opposed to clinical data, primarily due to the lack of extensive clinical data. Acquiring clinical data poses

its own challenges, especially since it is inherently challenging to acquire joint force or cartilage stress distribution from in-vivo studies. Despite these issues, using manual methods as a standard is in line with current research practices and provides a practical baseline for evaluating automated techniques against the accepted status quo in biomechanical studies.

Another limitation of this study is the simplification used in the FE model to demonstrate the performance of the automated attachment site identification algorithm, particularly the use of a linear elastic model for the cartilage instead of more sophisticated or subject-specific material models. This choice was driven by the need to maintain manageable computational times, especially given the number of models analyzed. However, this simplification does not critically impact the primary aim of this study, which was to assess the similarity between manual and automated methods for identifying attachment sites, rather than to study the precise long-term dynamic behavior of cartilage under load. The consistent use of a similar linear elastic model across all comparisons effectively satisfies our study's requirements, while balancing computational efficiency with the need for comparative accuracy.

The use of automated algorithms is especially useful in scenarios where time efficiency and scalability are crucial, such as in large-scale clinical or research studies where manual methods would be impractical due to their labor-intensive nature. In the current study, we used manually segmented bones and cartilages to better match the traditional manual workflow and to prevent the potential smoothing induced errors from automated segmentation from compound with attachment site identification. However, the automated attachment site identification algorithm can readily be coupled with automated segmentation, producing FE-ready models from MR scans in a matter of minutes. Additionally, this automated method paves the way for generating sufficient numbers of musculoskeletal models with labeled attachment sites, to be used as

training data for a machine learning algorithm. Future studies could explore the integration of these approaches for the development of a machine learning algorithm that could generate the musculoskeletal model for the entire knee, including bones, cartilages, and muscle and ligament attachment locations, directly from MR images.

This study demonstrates that automated identification of attachment sites is a viable and efficient alternative to manual methods, capable of supporting the high demands of modern biomechanical research and clinical practice. The similar performances of manual and automated methods in our study are encouraging for the field of computational biomechanics. By enabling faster and more scalable model development, automated methods hold the potential to transform the development of personalized, accurate, and reproducible musculoskeletal models, paving the way for their broader application in clinical diagnostics, treatment planning, and research.

ACKNOWLEDGEMENTS:

This material is based upon work supported by the National Science Foundation under Grant No. 1944180 and National Science Foundation Graduate Research Fellowship under Grant No. 1946726. We acknowledge support from the Institutional Development Awards (IDeA) from the National Institute of General Medical Sciences of the National Institutes of Health under Grants P20GM109095 and P30GM154497. The content is solely the responsibility of the authors and does not necessarily represent the official views of NIH.

Data and/or research tools used in the preparation of this manuscript were obtained and analyzed from the controlled access datasets distributed from the Osteoarthritis Initiative (OAI), a data repository housed within the NIMH Data Archive (NDA). OAI is a collaborative informatics

system created by the National Institute of Mental Health and the National Institute of Arthritis, Musculoskeletal and Skin Diseases (NIAMS) to provide a worldwide resource to quicken the pace of biomarker identification, scientific investigation and OA drug development. Dataset identifier(s): 1200285; 1200816.

CONFLICT OF INTEREST STATEMENT:

There are no conflicts of interest in this project from any of the authors.

REFERENCES:

Ali, A.A., Harris, M.D., Shalhoub, S., Maletsky, L.P., Rullkoetter, P.J., Shelburne, K.B., 2017. Combined measurement and modeling of specimen-specific knee mechanics for healthy and ACL-deficient conditions. Journal of Biomechanics 57, 117–124.

Ambellan, F., Tack, A., Ehlke, M., Zachow, S., 2019. Automated segmentation of knee bone and cartilage combining statistical shape knowledge and convolutional neural networks: Data from the Osteoarthritis Initiative. Medical Image Analysis 52, 109–118.

Baldwin, M.A., Clary, C.W., Fitzpatrick, C.K., Deacy, J.S., Maletsky, L.P., Rullkoetter, P.J., 2012. Dynamic finite element knee simulation for evaluation of knee replacement mechanics. Journal of Biomechanics 45, 474–483.

Burton, W., Myers, C., Rullkoetter, P., 2020. Semi-supervised learning for automatic segmentation of the knee from MRI with convolutional neural networks. Computer Methods and Programs in Biomedicine 189, 105328.

Cooper, R.J., Wilcox, R.K., Jones, A.C., 2019. Finite element models of the tibiofemoral joint: A review of validation approaches and modelling challenges. Medical Engineering and Physics 74, 1–12.

Cooper, R.J., Williams, S., Mengoni, M., Jones, A.C., 2018. Patient-specific parameterised cam geometry in finite element models of femoroacetabular impingement of the hip. Clinical Biomechanics 54, 62–70.

Dagneaux, L., Canovas, F., Jourdan, F., 2024. Finite element analysis in the optimization of posterior-stabilized total knee arthroplasty. Orthopaedics & Traumatology: Surgery & Research 110, 103765.

Diamond, L.E., Grant, T., Uhlrich, S.D., 2024. Osteoarthritis year in review 2023: Biomechanics. Osteoarthritis and Cartilage 32, 138–147.

Ebrahimkhani, S., Jaward, M.H., Cicuttini, F.M., Dharmaratne, A., Wang, Y., de Herrera, A.G.S., 2020. A review on segmentation of knee articular cartilage: from conventional methods towards deep learning. Artificial Intelligence in Medicine 106, 101851.

Ellis, B.J., Drury, N.J., Moore, S.M., McMahon, P.J., Weiss, J.A., Debski, R.E., 2010. Finite element modelling of the glenohumeral capsule can help assess the tested region during a clinical exam. Computer Methods in Biomechanics and Biomedical Engineering 13, 413–418.

Erdemir, A., Besier, T.F., Halloran, J.P., Imhauser, C.W., Laz, P.J., Morrison, T.M., Shelburne, K.B., 2019. Deciphering the “Art” in Modeling and Simulation of the Knee Joint: Overall Strategy. Journal of Biomechanical Engineering 141, 1–10.

Esrafilian, A., Chandra, S.S., Gatti, A.A., Nissi, M., Mustonen, A.-M., Säisänen, L., Reijonen, J., Nieminen, P., Julkunen, P., Töyräs, J., Saxby, D.J., Lloyd, D.G., Korhonen, R.K., 2023. An

Automated and Robust Tool for Musculoskeletal and Finite Element Modeling of the Knee Joint. bioRxiv 2023.10.14.562320. https://doi.org/10.1101/2023.10.14.562320

Farahmand, F., Naghi Tahmasbi, M., Amis, A., 2004. The contribution of the medial retinaculum and quadriceps muscles to patellar lateral stability—an in-vitro study. The Knee 11, 89–94.

Farahmand, F., Tahmasbi, M.N., Amis, A.A., 1998. Lateral force–displacement behaviour of the human patella and its variation with knee flexion — a biomechanical study in vitro. Journal of Biomechanics 31, 1147–1152.

Fitzpatrick, C.K., Baldwin, M.A., Clary, C.W., Maletsky, L.P., Rullkoetter, P.J., 2014. Evaluating knee replacement mechanics during ADL with PID-controlled dynamic finite element analysis. Computer Methods in Biomechanics and Biomedical Engineering 17, 360–369.

Fitzpatrick, C.K., Clary, C.W., Rullkoetter, P.J., 2012. The role of patient, surgical, and implant design variation in total knee replacement performance. Journal of Biomechanics 45, 2092–2102.

Gibbons, K.D., Clary, C.W., Rullkoetter, P.J., Fitzpatrick, C.K., 2019. Development of a statistical shape-function model of the implanted knee for real-time prediction of joint mechanics. Journal of Biomechanics 88, 55–63.

Gibbons, K.D., Malbouby, V., Alvarez, O., Fitzpatrick, C.K., 2022. Robust automatic hexahedral cartilage meshing framework enables population-based computational studies of the knee. Frontiers in Bioengineering and Biotechnology 10, 1–14.

Giorgino, T., 2009. Computing and Visualizing Dynamic Time Warping Alignments in R : The dtw Package. Journal of Statistical Software 31.

Grood, E.S., Suntay, W.J., 1983. A Joint Coordinate System for the Clinical Description of Three-Dimensional Motions: Application to the Knee. Journal of Biomechanical Engineering 105, 136–144.

Gulzar, H.M., 2018. Comprehensive Guide to Dynamic Time Warping in Python. LAMBERT Academic Publishing.

Harlaar, J., Macri, E.M., Wesseling, M., 2022. Osteoarthritis year in review 2021: mechanics. Osteoarthritis and Cartilage 30, 663–670.

Harris, M.D., Cyr, A.J., Ali, A.A., Fitzpatrick, C.K., Rullkoetter, P.J., Maletsky, L.P., Shelburne, K.B., 2016. A Combined Experimental and Computational Approach to Subject-Specific Analysis of Knee Joint Laxity. Journal of Biomechanical Engineering 138, 1–8.

Heinlein, B., Graichen, F., Bender, A., Rohlmann, A., Bergmann, G., 2007. Design, calibration and pre-clinical testing of an instrumented tibial tray. Journal of Biomechanics 40, S4–S10.

Khuyagbaatar, B., Kim, K., Kim, Y.H., 2024. Recent Developments in Finite Element Analysis of the Lumbar Spine. International Journal of Precision Engineering and Manufacturing 25, 487–496.

Klets, O., Mononen, M.E., Tanska, P., Nieminen, M.T., Korhonen, R.K., Saarakkala, S., 2016. Comparison of different material models of articular cartilage in 3D computational modeling of the knee: Data from the Osteoarthritis Initiative (OAI). Journal of Biomechanics 49, 3891–3900.

Kutzner, I., Heinlein, B., Graichen, F., Bender, A., Rohlmann, A., Halder, A., Beier, A., Bergmann, G., 2010. Loading of the knee joint during activities of daily living measured in vivo in five subjects. Journal of Biomechanics 43, 2164–2173.

Lochner, S.J., Huissoon, J.P., Bedi, S.S., 2014. Development of a patient-specific anatomical foot model from structured light scan data. Computer Methods in Biomechanics and Biomedical Engineering 17, 1198–1205.

Mononen, M.E., Paz, A., Liukkonen, M.K., Turunen, M.J., 2023. Atlas-based finite element analyses with simpler constitutive models predict personalized progression of knee osteoarthritis: data from the osteoarthritis initiative. Scientific Reports 13, 8888.

Mononen, M.E., Tanska, P., Isaksson, H., Korhonen, R.K., 2016. A novel method to simulate the progression of collagen degeneration of cartilage in the knee: Data from the osteoarthritis initiative. Scientific Reports 6, 1–14.

Müller, M., 2007. Dynamic Time Warping, in: Information Retrieval for Music and Motion. Springer Berlin Heidelberg, Berlin, Heidelberg, pp. 69–84.

Naghibi Beidokhti, H., Janssen, D., van de Groes, S., Hazrati, J., Van den Boogaard, T., Verdonschot, N., 2017. The influence of ligament modelling strategies on the predictive capability of finite element models of the human knee joint. Journal of Biomechanics 65, 1–11.

Ng, K.C.G., Lamontagne, M., Labrosse, M.R., Beaulé, P.E., 2016. Hip Joint Stresses Due to Cam-Type Femoroacetabular Impingement: A Systematic Review of Finite Element Simulations. PLOS ONE 11, e0147813.

Ng, K.C.G., Rouhi, G., Lamontagne, M., Beaulé, P.E., 2012. Finite Element Analysis Examining the Effects of Cam FAI on Hip Joint Mechanical Loading Using Subject-Specific Geometries During Standing and Maximum Squat. HSS Journal ® 8, 206–212.

NIAMS, N.I. of A. and M. and S.D., 2004. Osteoarthritis initiative (OAI): A knee Health study (clinical trial registration No. NCT00080171). Bethesda, Maryland.

Paz, A., Orozco, G.A., Korhonen, R.K., García, J.J., Mononen, M.E., 2021. Expediting finite element analyses for subject-specific studies of knee osteoarthritis: A literature review. Applied Sciences (Switzerland) 11.

Pfeiffer, F., 2016. The Use of Finite Element Analysis to Enhance Research and Clinical Practice in Orthopedics. Journal of Knee Surgery 29, 149–158.

Phan, P.K., Vo, A.T.N., Bakhtiarydavijani, A., Burch, R., Smith, B., Ball, J.E., Chander, H., Knight, A., Prabhu, R.K., 2021. In Silico Finite Element Analysis of the Foot Ankle Complex Biomechanics: A Literature Review. Journal of Biomechanical Engineering 143.

Rieger, L.K., Shah, A., Schick, S., Draper, D.B., Cutlan, R., Peldschus, S., Stemper, B.D., 2024. Subject-Specific Geometry of FE Lumbar Spine Models for the Replication of Fracture Locations Using Dynamic Drop Tests. Annals of Biomedical Engineering 52, 816–831.

Taylor, M., Bryan, R., Galloway, F., 2013. Accounting for patient variability in finite element analysis of the intact and implanted hip and knee: A review. International Journal for Numerical Methods in Biomedical Engineering 29, 273–292.

Virtanen, P., Gommers, R., Oliphant, T.E., Haberland, M., Reddy, T., Cournapeau, D., Burovski, E., Peterson, P., Weckesser, W., Bright, J., van der Walt, S.J., Brett, M., Wilson, J., Millman, K.J., Mayorov, N., Nelson, A.R.J., Jones, E., Kern, R., Larson, E., Carey, C.J., Polat, İ., Feng, Y., Moore, E.W., VanderPlas, J., Laxalde, D., Perktold, J., Cimrman, R., Henriksen, I., Quintero, E.A., Harris, C.R., Archibald, A.M., Ribeiro, A.H., Pedregosa, F., van Mulbregt, P., Vijaykumar, A., Bardelli, A. Pietro, Rothberg, A., Hilboll, A., Kloeckner, A., Scopatz, A., Lee, A., Rokem, A., Woods, C.N., Fulton, C., Masson, C., Häggström, C., Fitzgerald, C., Nicholson, D.A., Hagen, D.R., Pasechnik, D. V., Olivetti, E., Martin, E., Wieser, E., Silva, F., Lenders, F., Wilhelm, F., Young, G., Price, G.A., Ingold, G.-L., Allen, G.E., Lee, G.R., Audren, H., Probst, I., Dietrich, J.P., Silterra, J., Webber, J.T., Slavič, J., Nothman, J., Buchner, J., Kulick, J., Schönberger, J.L., de Miranda Cardoso, J.V., Reimer, J., Harrington, J., Rodríguez, J.L.C., Nunez-Iglesias, J., Kuczynski, J., Tritz, K., Thoma, M., Newville, M., Kümmerer, M., Bolingbroke, M., Tartre, M., Pak, M., Smith, N.J., Nowaczyk, N., Shebanov, N., Pavlyk, O., Brodtkorb, P.A., Lee, P., McGibbon, R.T., Feldbauer, R., Lewis, S., Tygier, S., Sievert, S., Vigna, S., Peterson, S., More, S., Pudlik, T., Oshima, T., Pingel, T.J., Robitaille, T.P., Spura, T., Jones, T.R., Cera, T., Leslie, T., Zito, T., Krauss, T., Upadhyay, U., Halchenko, Y.O., Vázquez-Baeza, Y., 2020. SciPy 1.0: fundamental algorithms for scientific computing in Python. Nature Methods 17, 261–272.

Wang, B., Mao, Z., Guo, J., Yang, J., Zhang, S., 2023. The non-invasive evaluation technique of patellofemoral joint stress: a systematic literature review. Frontiers in Bioengineering and Biotechnology 11.

Worsley, P., Stokes, M., Taylor, M., 2011. Predicted knee kinematics and kinetics during functional activities using motion capture and musculoskeletal modelling in healthy older people. Gait & Posture 33, 268–273.

Zheng, M., Zou, Z., Bartolo, P. jorge D. silva, Peach, C., Ren, L., 2017. Finite element models of the human shoulder complex: a review of their clinical implications and modelling techniques. International Journal for Numerical Methods in Biomedical Engineering 33.

Zhou, Q.-Y., Park, J., Koltun, V., 2018. Open3D: A Modern Library for 3D Data Processing.

List of Figures:

Figure 1. Muscle and ligament structures included in the FE model.

Figure 2. The attachment site identification process. (A) the template model is built based on experimental dissection and probing, and anatomical landmarks, (B) the subject-specific model is built based on knee MRI, (C) the subject-specific model is scaled in medial-lateral and anterior-posterior directions and superimposed on the template, (D) for each attachment site, the nearby template anchor points are found, (E) for template anchor point, the equivalent subject anchor point is determined, (F) subject model scaled back to original size, (G) the vectors going from the template anchor points to the attachment site are determined, (H) these vectors are projected to their equivalent subject anchor point after scaling, (I) the weighted average of vector endpoints is calculated based on distance from the attachment site, (J) the subject attachment site is determined, (K) this process repeated for all attachment sites makes the subject specific musculoskeletal model.

Figure 3. The local anatomical landmarks and coordinate system automatically determined, (A) most distal points on medial and lateral femoral condyles, (B) dwell points on medial and lateral tibial condyles, (C) medial and lateral tibial intercondylar tubercles, (D) Grood and Suntay axes for the knee.

Figure 4. Flowchart of the overall study design. RMSE: root mean squared error, DTW: dynamic time warping, MRI: magnetic resonance image, FE: finite element, CC: correlation coefficient

Figure 5. (A) The FE model of a deep knee bend activity, (B) von Mises stress in tibial and patellar cartilages in full extension and (C) at maximum flexion.

Figure 6. The between-condition comparison for the distances between attachment site nodal locations. E1: Evaluator 1, E2: Evaluator 2, Au: Auto

Figure 7. Similarity between conditions across all output variables based on an RMSE-based similarity index (left) and Pearson Correlation Coefficient (right). Each bar (slice) represents the similarity between the two manual models for a given variable, with the variable indices shown around the plot. The length of each bar was computed by averaging the relative index across all subjects for that variable. Red and blue markers indicate the similarity between the automated model and the manual models from evaluator 1 (red) and evaluator 2 (blue). The colors of the bars are used solely for visual distinction between variables and do not represent any specific value. The RMSE-based similarity index was calculated for plotting purposes by first normalizing the RMSE values via dividing them by their maximum value, and then reversed so that higher scores denote greater similarity between the conditions. The complete list of variables and their raw and normalized RMSE values can be found in Appendix 1. * A significant

564 difference between pairwise comparisons was found only for patellofemoral medial-lateral
565 translation (variable 13) as denoted by an asterisk.

566

567 **Figure 8.** Average kinematic outputs across all subjects (showing a representative sample of
568 kinematic outputs), with shaded regions illustrating the 25th and 75th percentile for each
569 condition. A-P: anterior-posterior, M-L: medial-lateral, I-E: internal-external, V-V: varus-valgus,
570 S-I: superior-inferior.

571

572 **Figure 9.** Mean force and contact outputs across all subjects (showing a representative sample of
573 soft-tissue forces, contact areas, joint forces and center of pressure outputs), with shaded regions
574 illustrating the 25th and 75th percentile for each condition. CoP: center of pressure, PAT: patellar
575 cartilage, TIB_MED: tibial medial cartilage. A-P: anterior-posterior, M-L: medial-lateral. Note:
576 The mean ACL total force is higher than the 75th percentile for a portion of the cycle because the
577 mid-cycle ACL force drops to zero in several knees, skewing the 75th percentile lower than the
578 mean.

579

580 **Figure 10.** Average 90th percentile first principal logarithmic strain, and 50th and 95th percentile
581 von Mises stress across all subjects, with shaded regions illustrating the 25th and 75th percentile
582 for each condition. FEM: femoral cartilage, PAT: patellar cartilage, TIB_MED: tibial medial
583 cartilage.

584

585

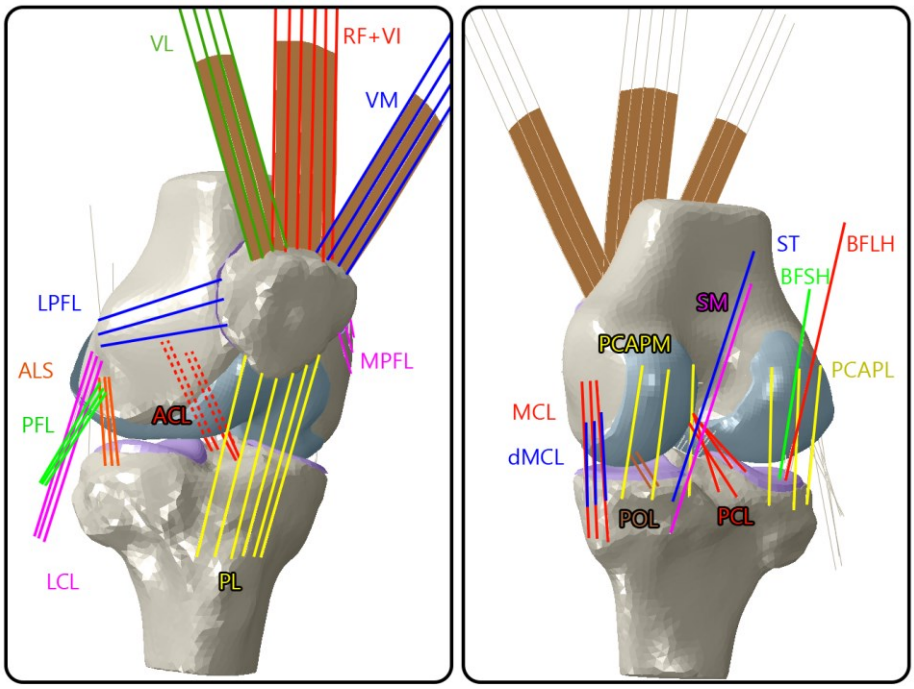

Figure 1. Muscle and ligament structures included in the FE model.

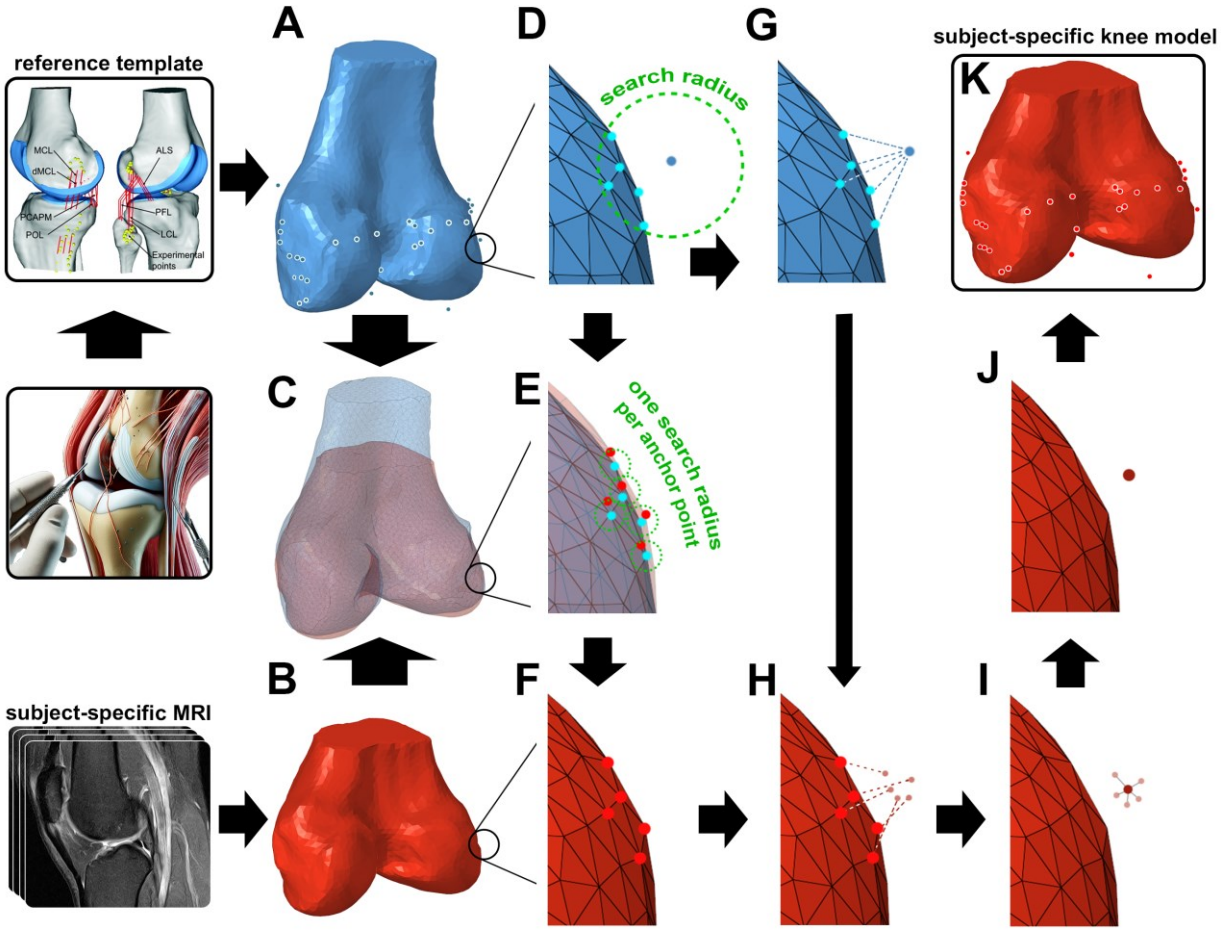

Figure 2. The attachment site identification process. (A) the template model is built based on experimental dissection and probing, and anatomical landmarks, (B) the subject-specific model is built based on knee MRI, (C) the subject-specific model is scaled and superimposed on the template, (D) for each attachment site, the nearby template anchor points are found, (E) for template anchor point, the equivalent subject anchor point is determined, (F) subject model scaled back to original size, (G) the vectors going from the template anchor points to the attachment site are determined, (H) these vectors are projected to their equivalent subject anchor point after scaling, (I) the weighted average of vector endpoints is calculated based on distance from the attachment site, (J) the subject attachment site is determined, (K) this process repeated for all attachment sites makes the subject specific musculoskeletal model.

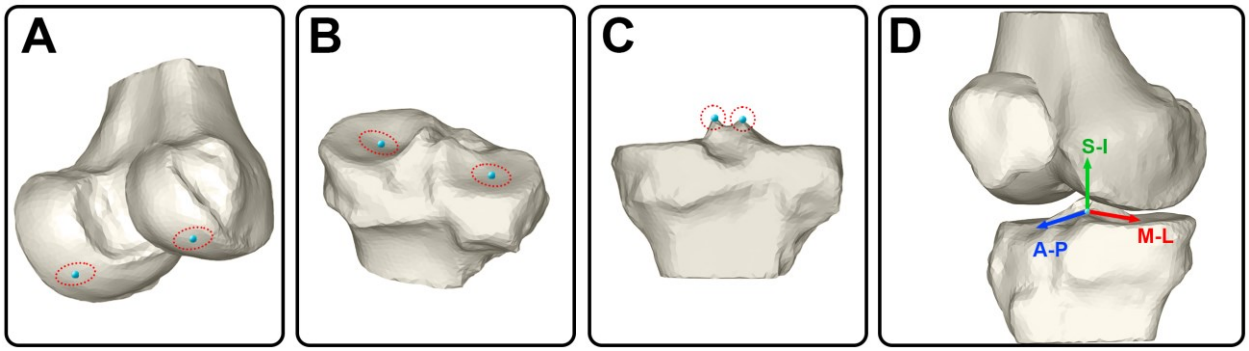

Figure 3. The local anatomical landmarks and coordinate system automatically determined, (A) most distal points on medial and lateral femoral condyles, (B) dwell points on medial and lateral tibial condyles, (C) medial and lateral tibial intercondylar tubercles, (D) Grood and Suntay axes for the knee.

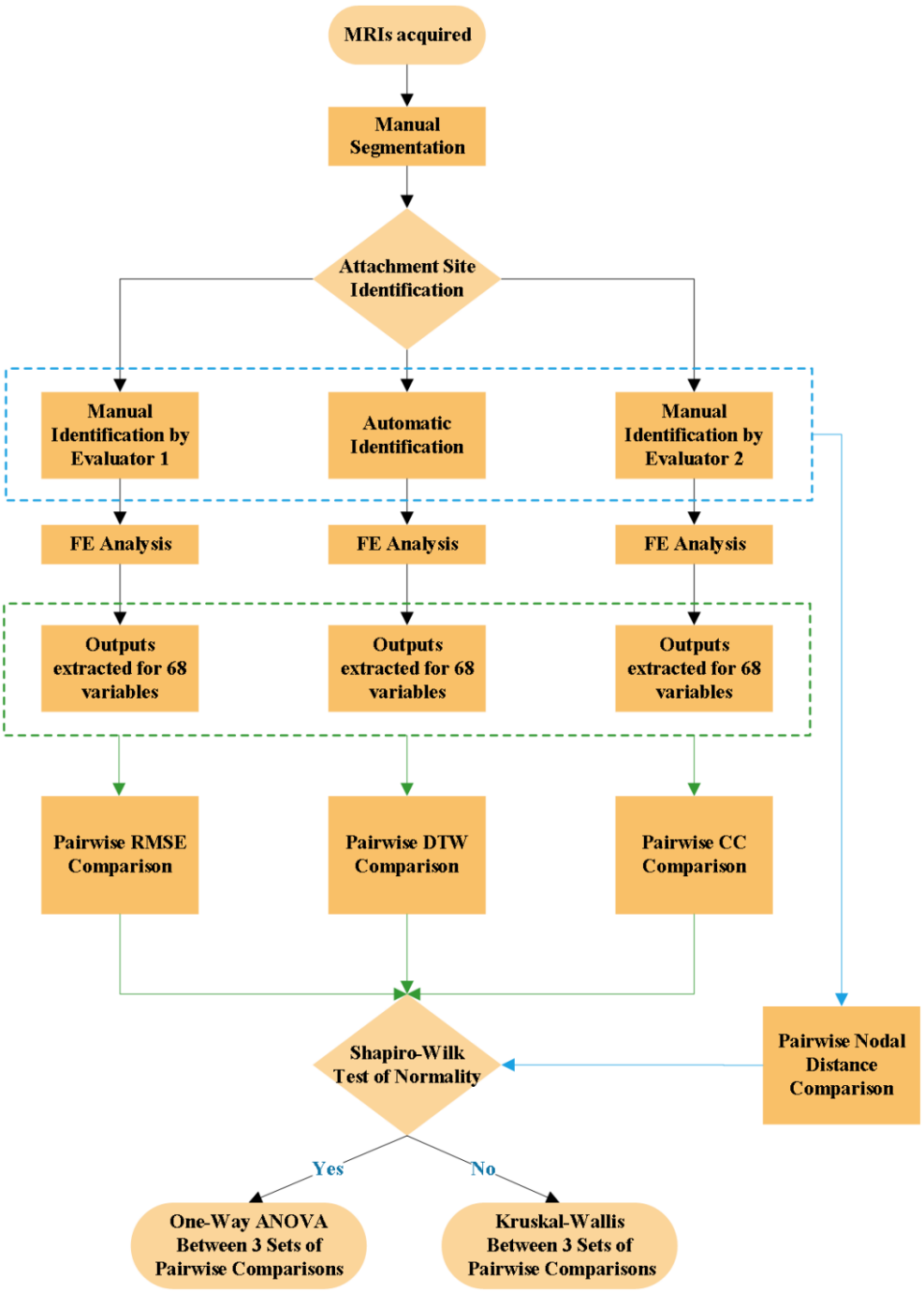

634

635 **Figure 4.** Flowchart of the overall study design. RMSE: root mean squared error, DTW:

636 dynamic time warping, MRI: magnetic resonance image, FE: finite element, CC: correlation

637 coefficient

638

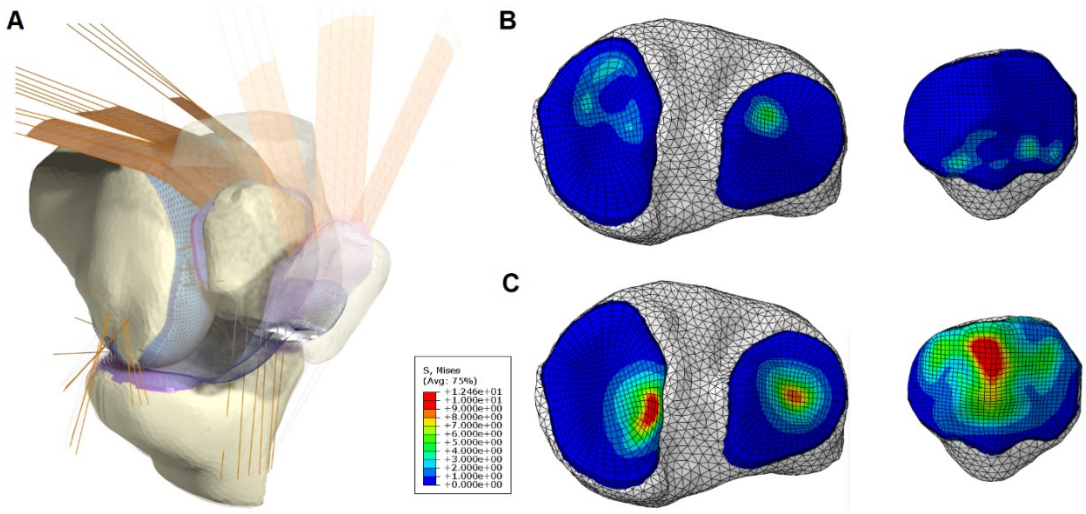

639

640 **Figure 5.** (A) The FE model of a deep knee bend activity, (B) von Mises stress in tibial and

641 patellar cartilages in full extension and (C) at maximum flexion.

642

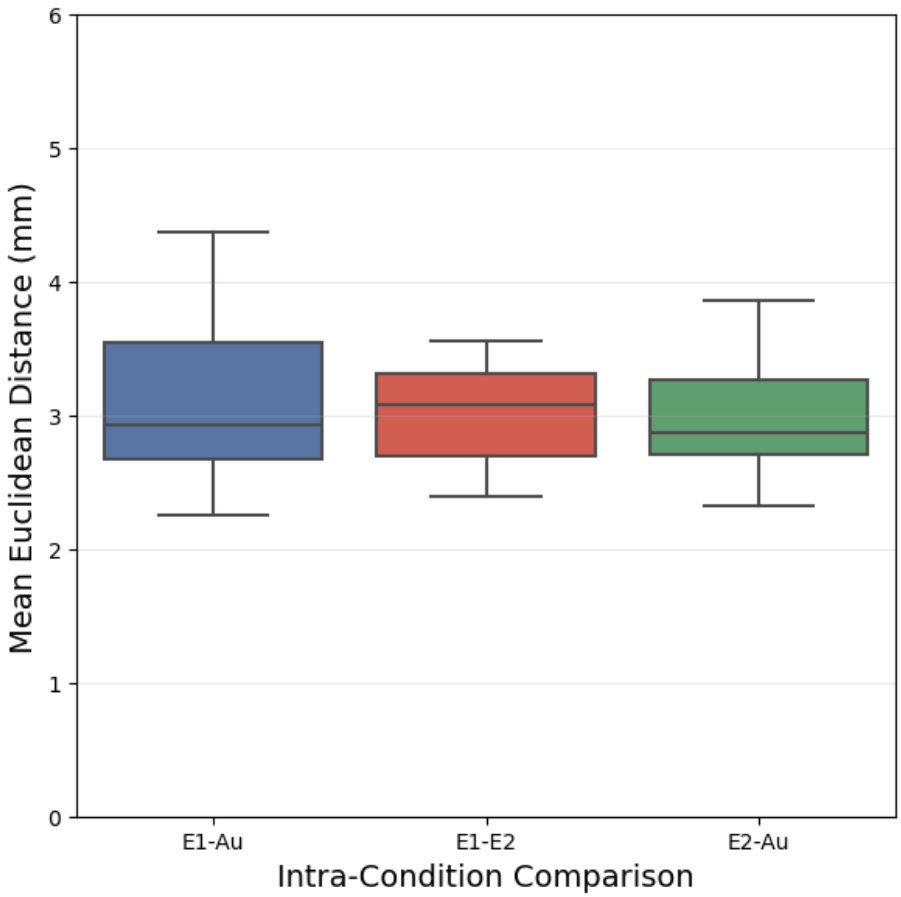

643

644 **Figure 6.** The between-condition comparison for the distances between attachment site nodal

645 locations. E1: Evaluator 1, E2: Evaluator 2, Au: Auto

646

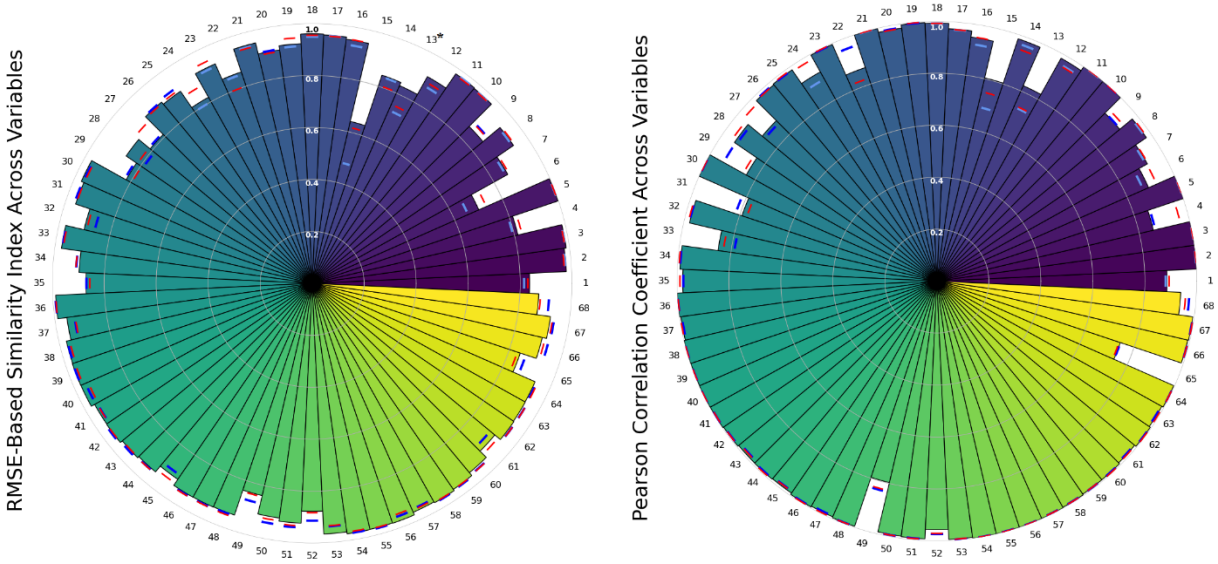

Figure 7. Similarity between conditions across all output variables based on an RMSE-based similarity index (left) and Pearson Correlation Coefficient (right). Each bar (slice) represents the similarity between the two manual models for a given variable, with the variable indices shown around the plot. The length of each bar was computed by averaging the relative index across all subjects for that variable. Red and blue markers indicate the similarity between the automated model and the manual models from evaluator 1 (red) and evaluator 2 (blue). The colors of the bars are used solely for visual distinction between variables and do not represent any specific value. The RMSE-based similarity index was calculated for plotting purposes by first normalizing the RMSE values via dividing them by their maximum value, and then reversed so that higher scores denote greater similarity between the conditions. The complete list of variables and their raw and normalized RMSE values can be found in Appendix 1. * A significant difference between pairwise comparisons was found only for patellofemoral medial-lateral translation (variable 13) as denoted by an asterisk.

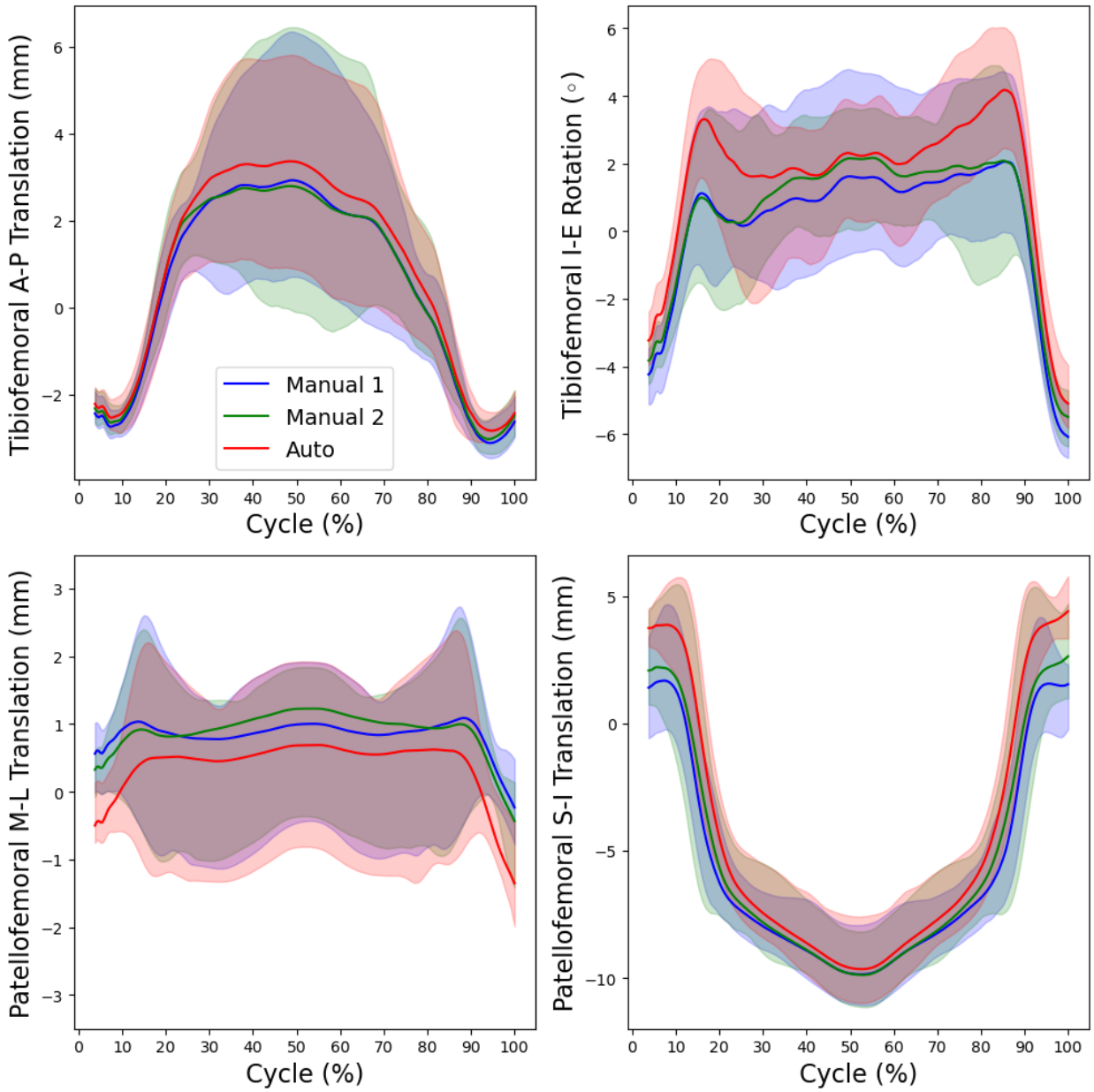

Figure 8. Average kinematic outputs across all subjects (showing a representative sample of kinematic outputs), with shaded regions illustrating the 25th and 75th percentile for each condition. A-P: anterior-posterior, M-L: medial-lateral, I-E: internal-external, V-V: varus-valgus, S-I: superior-inferior.

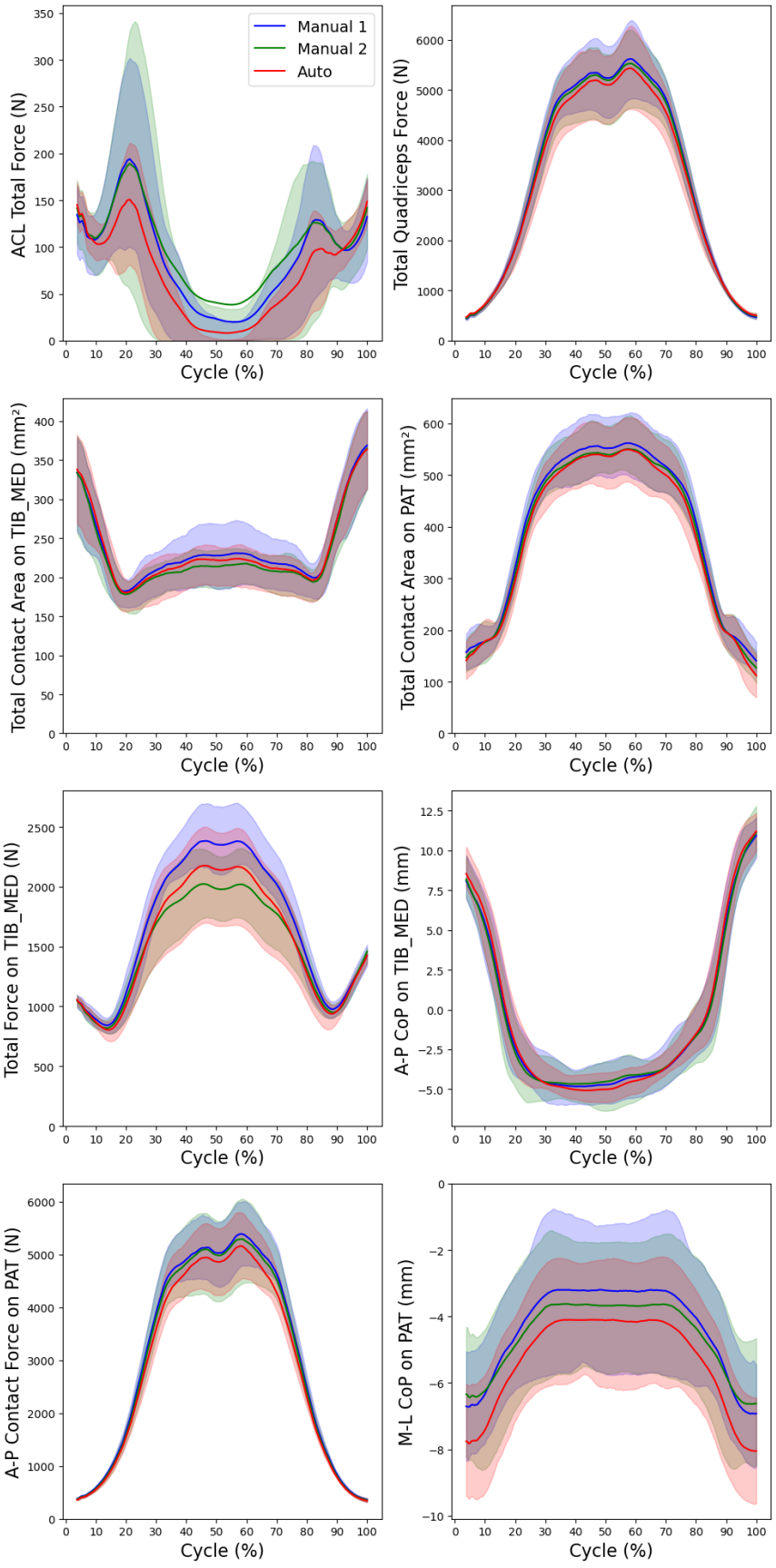
Manual 1
Manual 2
Auto
ACL Total Force (N)
Total Quadriceps Force (N)
Total Contact Area on TIB_MED (mm²)
Total Contact Area on PAT (mm²)
Total Force on TIB_MED (N)
A-P CoP on TIB_MED (mm)
A-P Contact Force on PAT (N)
M-L CoP on PAT (mm)
Cycle (%)

668

Figure 9. Mean force and contact outputs across all subjects (showing a representative sample of soft-tissue forces, contact areas, joint forces and center of pressure outputs), with shaded regions illustrating the 25th and 75th percentile for each condition. CoP: center of pressure, PAT: patellar cartilage, TIB_MED: tibial medial cartilage. A-P: anterior-posterior, M-L: medial-lateral. Note: The mean ACL total force is higher than the 75th percentile for a portion of the cycle because the mid-cycle ACL force drops to zero in several knees, skewing the 75th percentile lower than the mean.

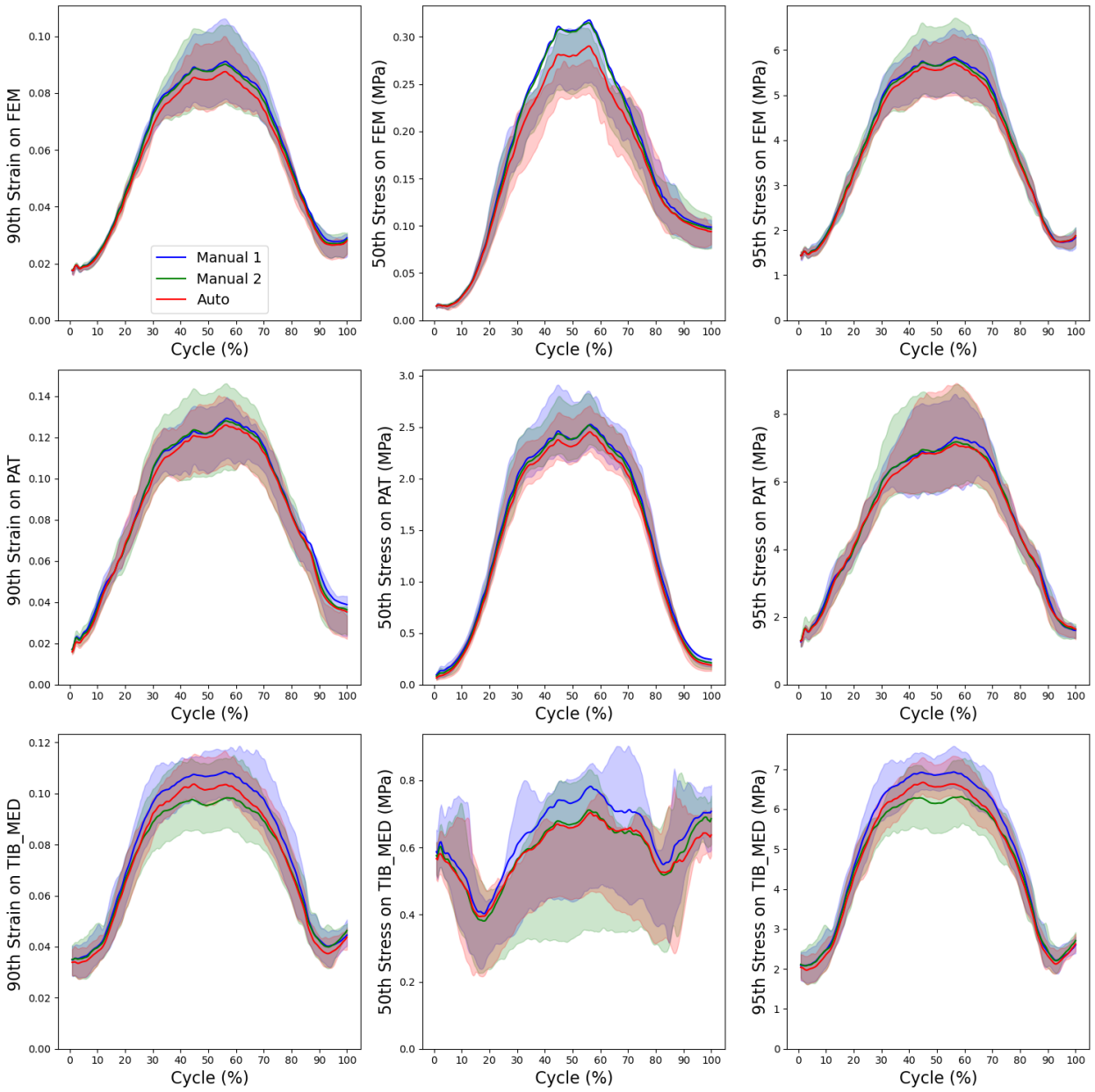

695

696 **Figure 10.** Average 90th percentile first principal logarithmic strain, and 50th and 95th percentile

697 von Mises stress across all subjects, with shaded regions illustrating the 25th and 75th percentile

698 for each condition. FEM: femoral cartilage, PAT: patellar cartilage, TIB_MED: tibial medial

699 cartilage